MHD Mode Composition in the Inner Heliosphere from the *Parker Solar Probe*'s First Perihelion

C. C. Chaston[1], J. W. Bonnell[1], S. D. Bale[1,2,3], J. C. Kasper[4,5], M. Pulupa[1], T. Dudok de Wit[6], T. A. Bowen[1], D. E. Larson[1], P. L. Whittlesey[1], J. R. Wygant[7], C. S. Salem[1], R. J. MacDowall[8], R. L. Livi[1], D. Vech[4], A. W. Case[5], M. L. Stevens[5], K. E. Korreck[5], K. Goetz[7], P. R. Harvey[1], and D. M. Malaspina[9]

[1] Space Science Laboratory, University of California, Berkeley, CA 94720-7450, USA; ccc@ssl.berkeley.edu
[2] Physics Department, University of California, Berkeley, CA 94720-7300, USA
[3] The Blackett Laboratory, Imperial College London, London, SW7 2AZ, UK
[4] Climate and Space Sciences and Engineering, University of Michigan, Ann Arbor, MI 48109, USA
[5] Smithsonian Astrophysical Observatory, Cambridge, MA 02138, USA
[6] LPC2E, CNRS and University of Orleans, Orleans, France
[7] School of Physics and Astronomy, University of Minnesota, Minneapolis, MN, USA
[8] Solar System Exploration Division, NASA/Goddard Space Flight Center, Greenbelt, MD 20771, USA
[9] Laboratory for Atmospheric and Space Physics, University of Colorado, Boulder, CO 80303, USA

Abstract

Field and plasma variations during the first perihelion pass of the *Parker Solar Probe* (*PSP*) from 53 into 35 solar radii (R_S) from the Sun and over a frequency range in the spacecraft frame (f_{SC}) from 0.0002 to 0.2 Hz are decomposed into constituent magnetohydrodynamic (MHD) modes. The analysis operates on measurements of the MHD variables recorded between impulsive, large amplitude rotations of the magnetic field to reveal the dominance of a broad spectrum of shear Alfvén waves propagating antiparallel (backward) to the background magnetic field ($\boldsymbol{B}_0$) with a significant fraction of spectral energy density in the backward slow mode and, to a lesser extent, fast mode waves. While all three MHD modes provide Poynting flux directed outward from the Sun the impulsive rotations of B_0 from inward to outward radial orientations provide intervals of outward and inward propagation in the plasma frame, respectively. This morphology is suggestive of outward wave propagation from a near Sun source along kinked field lines that provide alternating radial B_0 orientations as the magnetic field is advected with the flow over the spacecraft. Shear Alfvén and slow mode spectral energy density is generally largest within intervals of reversed radial B_0, while the fast mode tends to occur outside these regions, albeit with lower intensity. The spectral energy density in the forward propagating modes increases with f_{SC} above 0.01 Hz, which is suggestive of back scatter in the plasma frame of the dominant backward modes from the radial field reversals and associated inhomogeneities of the embedded plasmas.

Unified Astronomy Thesaurus concepts: Magnetohydrodynamics (1964); Slow solar wind (1873); Solar coronal holes (1484)

1. Introduction

Resolving the composition and propagation properties of magnetohydrodynamic (MHD) field variations in solar wind plasmas is needed to advance understanding of the heating and acceleration of the solar wind (Roberts 2010; Ofman 2016). These modes transport energy outward from the Sun in the form of Poynting flux (Belcher & Davis 1971; Mozer et al. 2020) and drive the acceleration of energetic particle populations (e.g., Liu et al. 2004), while powering turbulent cascades down to kinetic scales at which heating of the plasma may occur (Leamon et al. 1999; Chandran et al. 2010; Chen et al. 2019). While extensive in situ observations have been performed at 1 au (e.g., Yao et al. 2011; Howes et al. 2012; Shi et al. 2015) and measurements from *Helios* (Marsch & Tu 1990; Tu & Marsch 1994), *Ulysses* (Balogh et al. 1992; Bavassano et al. 2004), and *Messenger* (Gerschmann et al. 2012) have explored MHD wave turbulence all the way into 0.29 au, the penetration of the *Parker Solar Probe* (*PSP*) deep into the inner heliosphere allows an assessment of the wave mode composition near the source of the super-Alfvénic solar wind. At this location it may reasonably be expected that the relative contribution of the MHD modes, as well as their

morphology and propagation characteristics, differ from that observed at larger radial distances (Tu & Marsch 1995).

Analyses of field and plasma variations in the solar wind at radial distances beyond 0.29 au and low latitudes have indicated the preponderance of Alfvénic fluctuations (Bruno & Carbone 2005). Here correlated variation in magnetic fields and flow velocities transverse to the larger-scale magnetic field and, on temporal scales longer than the convection time of thermal ion gyro-radii, have been shown to represent a broad spectrum of radially outward propagating shear Alfvén waves (Belcher & Davis 1971). Compressive variations, generally comprising a small fraction of the total energy content, have been identified primarily as slow mode or pressure balance structures (Tu & Marsch 1995). Nonetheless, fluctuations consistent with fast mode oscillations have been reported during intervals of high-speed wind (Tu & Marsch 1994) and enhanced plasma beta, albeit at very low levels (Howes et al. 2012). Studies of the variation of the MHD variables with radial distance outward from 0.29 au have shown that Alfvénic correlation decreases with radial distance while contributions from variations in the mass density and magnetic field intensity increase (Bruno & Bavassano 1993). These observations indicate an increasing fraction of inward propagating and

compressive modes in the spectral composition with radial distance from the Sun (Bruno et al. 2006). Extrapolating this trend inward from 0.29 au suggests that MHD-scale field and plasma fluctuations observed from *PSP* during its first perihelion into 0.16 au should be especially Alfvénic in nature.

To investigate low-frequency wave properties in the inner heliosphere we apply an MHD model to the measured fluctuations in fields, flows and particle pressures returned from *PSP* and decompose the observed spectral energy density into shear Alfvén waves and fast and slow magnetosonic modes. The decomposition is performed by "filtering" the spectral matrix assembled from the MHD variables using eigenvectors defining the "polarization" state of the constituent wave modes (Glassmeier et al. 1995). The analysis exploits the high time resolution plasma and field survey measurements routinely available from the Faraday cup (Solar Probe Cup (SPC); Kasper et al. 2016) and magnetometer instruments (Fields; Bale et al. 2016) on board *PSP*. These measurements allow an examination of the spectral composition of the field and plasma fluctuations and wave mode propagation directions along the background magnetic field (B_0) into ∼0.16 au as explored by *PSP* during its first perihelion.

2. MHD Mode Decomposition

To determine the mode composition of the time series field and plasma fluctuations from *PSP*, a generalized spectral filtering approach is implemented with a single fluid MHD model as described by Glassmeier et al. (1995). In this model the orientation of the field-aligned wavevector ($k_\parallel$) parallel (forward) or antiparallel (backward) to B_0 is implicit in the relationship between the MHD variables b, v, and ρ, representing the fluctuating magnetic field, fluid velocity, and mass density, respectively. The phase speed of the constituent wave modes then depends only on the background plasma parameters and the propagation angle (θ_k) relative to B_0 defined over the range of $0 \leqslant \theta_k \leqslant \pi/2$. This allows estimates of the spectral composition to be derived without knowledge of the plasma frame frequency nor the magnitude of the wavevector. Consequently, single point measurements of field and plasma variations from *PSP* can be decomposed into constituent MHD modes if the MHD model appropriately describes the solar wind plasma and if θ_k can be determined.

Because the MHD decomposition operates on plane polarized waves, it does not appropriately characterize variations in the magnetic field shown to transcribe a sphere in magnetic field intensity as commonly observed in the solar wind (Tsurutani et al. 2018). These "spherically" polarized waves comprise rotations of the total field and often appear in observations from *PSP* as impulsive features leading to reversals of the radial magnetic field (Bale et al. 2019; Kasper et al. 2019; Horbury et al. 2020). The correlated magnetic field and flows in these features mean that the linear decomposition identifies them as mostly Alfvénic; however, as they are not strictly consistent with the model used, they are excluded from the composition statistics we report. These nonlinear features instead contribute the larger-scale background field topology in which the modes that the decomposition describes reside.

In the plane–wave approximation θ_k should be determined independently for each mode. However, the relationship between the MHD variables in forward and backward propagating shear Alfvén waves are invariant with θ_k—a property commonly exploited for the evaluation of Elsässer

variables (Bruno & Carbone 2016). If the MHD model appropriately describes the plasma, then θ_k primarily establishes what fraction of the non-Alfvénic spectral energy density resides in either the magnetosonic fast or slow modes. However, even for the magnetosonic modes the opposite phase relationship between plasma and field pressure that distinguishes fast from slow waves is independent of θ_k. This property is the basis of studies concerning the nature of compressive fluctuation in the solar wind (e.g., Shi et al. 2015). Consequently, for the purpose of estimating the relative spectral energy content in the forward and backward propagating MHD modes, the requirements on θ_k are quite modest. This fact has been demonstrated by application of the mode decomposition technique to synthetic data, where the orientation of k is known, by Glassmeier et al. (1995) and has been confirmed in the application to the *PSP* observations described below by examining the variation in the fractional composition with variations in θ_k.

The implementation of the decomposition approach to *PSP* observations begins by linearizing the magnetic field variations as $B = B_0 + b$ and defining a coordinate system at each frequency in the spacecraft frame (f_{Sc}) and time (t) in which $\nabla \cdot b = 0$ is enforced. Implicit in this analysis is the requirement that a definitive B_0 for each wave scale considered can be identified. To facilitate this analysis when $|b|/|B_0|$ can be ∼1 we implement a wavelet technique where B_0 is defined independently at the wave scale (or f_{SC}) being considered. A similar approach is implemented for variations in the mass density (ρ). For the compilation of statistics this approach allows for the removal of spectral estimates impacted by the impulsive magnetic field rotations that are characteristic of the radial field reversals observed from *PSP* and, as mentioned above, that are not appropriately described by a linear MHD model. More details will be provided when examining the observations in Section 3. The coordinate system is then organized by locating the unit vector defining the minimum variance direction (m) from the off-diagonal components of the spectral matrix in b at each f_{SC} and time (Samson & Olson 1980). The angle between B_0 and m is then $\theta_m = \mathrm{acos}(|m \cdot B_0/B_0|)$, which we will use as our estimate for θ_k. The spectral coefficients of the MHD variables are then arranged around m to form the state vector defined in Glassmeier et al. (1995) as

$$v = \frac{1}{v_A}\left[v_y, \frac{b_y}{\sqrt{\mu_o \rho_0}}, v_x, v_z, \frac{b_z}{\sqrt{\mu_o \rho_0}}, \frac{\rho c_S}{\rho_0} \right]^T, \qquad (1)$$

where the x coordinate lies along m and hence $b_x = 0$, and B_0, resides in the xz plane. Here v_A is the Alfvén speed, c_S is the acoustic speed, and ρ_0 the background mass density. The spectral matrix, S, describing the relationship between each of the MHD variables in the minimum variance coordinate system is then defined as

$$S = vv^*, \qquad (2)$$

where v^* is the Hermitian adjoint of v. From this matrix the contribution from each mode to the spectral energy density (defined by the trace of S) is then provided by "filtering" S as

$$|g_i(f_{sc}, t))|^2 = e_i^T S(f_{sc}, t) e_i. \qquad (3)$$

Here g_i is the complex coefficient for the ith mode, $|g_i(f_{sc}, t)|^2$ is the corresponding spectral energy density, and e_i is the

eigenvector describing the relationship between the MHD field and plasma variables for each mode. Here, it should be noted that g_i contains the total spectral energy density in all the MHD variables defined for each eigenvector—not just those in the flows and/or fields as often used to assess the contribution of compressive fluctuations relative to Alfvénic fluctuations (Bruno & Bavassano 1991; Chen et al. 2019). An analysis of the linearized single fluid MHD equations provides eigenvectors for $\boldsymbol{k}_\parallel \cdot \boldsymbol{B}_0 > 0$ and $\boldsymbol{k}_\parallel \cdot \boldsymbol{B}_0 < 0$ describing, respectively, the forward and backward propagating shear Alfvén, fast, and slow magnetosonic modes at each f_{SC} and t. For an easily accessible derivation of the eigenvectors we refer to Motschmann et al. (1998, see Equations 4.9–4.13) while noting a missing Alfvén speed factor in their normalization (Equation 4.13). Significantly, the forward and backward shear Alfvén modes can be rearranged into radially inward and outward propagating waves using the orientation of the radial component of $\boldsymbol{B}_0$. This provides quantities analogous to the Elsässer variables as often used to organize Alfvénic fluctuations in this context (e.g., Marsch & Tu 1990) and hence also facilitates evaluation of the cross helicity used to describe the balance of counter-propagation in studies of solar wind turbulence (Bruno & Carbone 2016; McManus et al. 2020).

Combined measurements from the Fields (Bale et al. 2016) and SPC (Kasper et al. 2016) instruments on board *PSP* provide the MHD variables required to define υ. As we do not yet have electron temperature (T_e) moments from the Solar Probe ANalysers (SPAN) instrument (Kasper et al. 2016) we take $T_e \sim T_i$ following the observational study by Richter & Marsch (1988) at 0.29 au while noting that the spectral composition will vary only slowly with deviations from this relationship. For easy description of the mode composition results we define the normalized or fractional composition,

$$\overline{g}_i^2 = |g_i(f_{sc}, t))|^2 \big/ Tr(S), \qquad (4)$$

where $\overline{g}_i^2$ quantifies the fraction of observed spectral energy density based on the full set of MHD variables (Equation (1)) that is consistent with each of the single fluid MHD modes. Here we note that because the solar wind velocity (v_{SW}) at *PSP* is, in general, significantly larger than MHD wave phase speeds, we have $f_{SC} \propto k$, so that for a given θ_k, the wave dispersion of each MHD mode at each f_{sc} identifies a single point in $\omega - k$ space (where ω is the plasma frame angular frequency). Consequently, no integration in this space is required. Further details specific to *PSP* data quantities are described below.

3. Observations

Through the implementation of the mode decomposition approach we have explored the MHD wave composition from $f_{SC} = 0.0002$ to $0.2\,\mathrm{Hz}$ over the first perihelion pass of *PSP* covering the radial range from 53 to 35 R_S. Defining ρ_i as the thermal ion gyro-radius the upper limit in f_{SC} maintains $k\rho_i < 1$, where $2\pi f_{SC} = \omega_{SC} \sim kv_{SW}$ for observed solar wind speeds (v_{SW}) and is everywhere less than the plasma frame proton cyclotron frequency. The lower limit in f_{SC} is defined by the inverse maximum period between the impulsive field rotations that lead to the radial field reversals characteristic of the interval under study (Bale et al. 2019) and to maintain
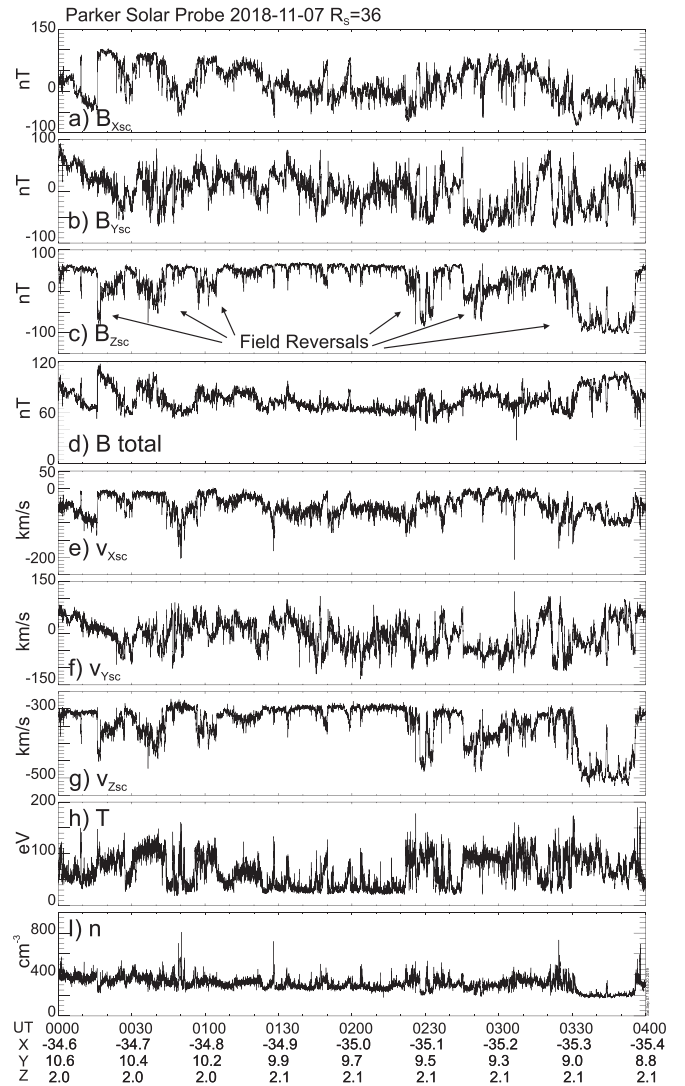

Figure 1. Time series variation in the MHD variables. Vector quantities are in spacecraft coordinates as defined in the text. (a)–(d) Time series measurements of the magnetic field from the Fields fluxgate magnetometer. (e)–(g) Proton drift velocity from the SPC instrument. (h) and (i) Proton temperature and density from SPC.

reasonable computation times. We note that the former necessarily means that statistics at lower f_{SC} are reduced. It also worth noting that a frequency of ~1 mHz has been suggested as the lower bound for MHD waves in the solar wind (Bruno & Carbone 2016) and the range in f_{SC} considered corresponds to what is usually defined as the "inertial range" of solar wind turbulence. The timespan of the analysis extends from 2018 October 31 until November 11 when the spacecraft was almost stationary in the rotating frame of the Sun. Over this interval the spacecraft was immersed in the "slow" solar wind and connected to a small equatorial coronal hole (Bale et al. 2019; Badman et al. 2020) with the gross magnetic field directed inward toward the Sun.

Figure 1 shows an interval of fields and plasma measurements recorded on 2018 November 7 at a radial distance of ~36 R_S. These data are presented in the spacecraft coordinate system where x_{sc} points perpendicular to the Sun–spacecraft line in the ecliptic plane and in the direction of solar rotation, y_{sc} is perpendicular to the ecliptic plane and pointing southward and z_{sc} points toward the Sun. These data include all the

measurements required to perform the MHD mode decomposition described above. The magnetometer data are the Survey Mode fluxgate magnetometer measurements routinely returned from *PSP* Fields instrument (Bale et al. 2019), while the particle measurements are provided by the Solar Wind Electrons Alphas and Protons instrument (SWEAP) in "Encounter Mode" and based on fits to the SPC measurements of the proton core (Kasper et al. 2019). For a description of these measurements we refer to the respective instrument papers and for details of the SPC data fitting routine, and uncertainties therein, we refer to the Case et al. (2020) and the "users" document available on the SWEAP website (http://sweap.cfa.harvard.edu/sweap_data_user_guide.pdf). Typical uncertainties over the interval considered are 0.09, 0.03, and 0.19 for the density, velocity, and temperature, respectively. These uncertainties are insufficient to provide differences in the composition results that are significant relative to the natural variation in the composition results discussed below. It is also noted that the combined effect of temperature anisotropy and rotations in the magnetic field alter the measured temperatures returned from the SPC instrument (Case et al. 2020; Huang et al. 2020) and constitute an additional source of uncertainty in the spectral composition estimates from the single fluid MHD model. Taking $T_\perp$ and $T_\parallel$ as, respectively, the temperatures perpendicular and parallel to the magnetic field an assessment of this effect for a nominal anisotropy of $\frac{T_\perp}{T_\parallel} = 1.5$ over the interval shown in Figure 1 defines a maximum uncertainty of $\lesssim 10\%$ in wave composition that is, in general, significantly less than the variations in wave composition observed. This uncertainty is primarily represented by changes in the relative fraction of fast to slow mode wave power. While the effect of the anisotropy at this nominal level is insufficient to significantly impact the results described below, it may become significant for the large anisotropy values sometimes observed.

The outstanding features in Figure 1 are the periods of radial field polarity rotation and reversal (Figure 1(c)), mentioned above, and correlated enhancements or "jets" in the plasma flow (Figure 1(f)). These intervals of impulsive field rotation, sometimes referred to as "switchbacks," are documented throughout the first *PSP* perihelion by Kasper et al. (2019), Bale et al. (2019), Dudok de Wit et al. (2020), and Horbury et al. (2020) and are featured in several other works in this special issue. The corotation of the spacecraft with the Sun over the range studied suggests that these features represent a largely radial structure advected over the spacecraft with the solar wind. This interpretation is supported by observations of the plasma mode composition that we now discuss.

Figure 2 shows results from the application of the mode decomposition methodology described above to the time series variations shown in Figure 1. For context the radial field variations from Figure 1 are again presented in Figure 2(a). Comparison of this time series to the corresponding trace power in the magnetic field fluctuations shown in Figure 2(b) indicates that enhancements in spectral energy density occur inside regions of reversed radial fields. The subsequent panels show θ_m and the fraction of observed spectral energy density estimated to reside in each of the six MHD modes. The spectral quantities shown in Figure 2 are produced using Morlet wavelets, although a windowed Fourier transform provides comparable output, albeit with reduced resolution at higher frequencies. The analysis begins with the rotation of the MHD variables from spacecraft coordinates to a field-aligned coordinate system where B_0 at
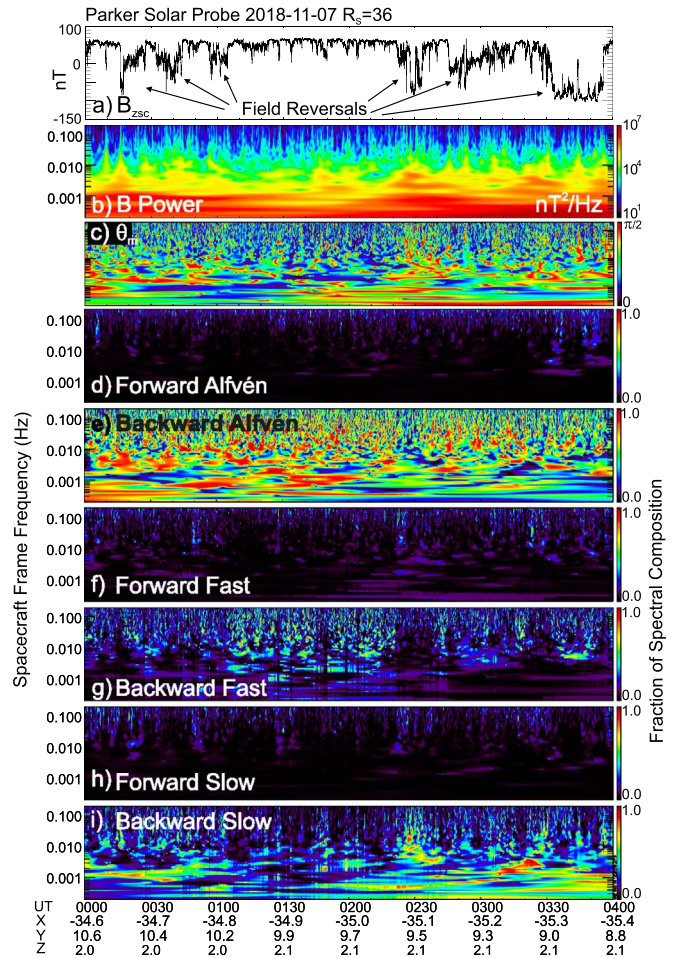

Figure 2. MHD mode decomposition on the 2018 November 7. (a) Radial component of the magnetic field with positive values pointing inward toward the Sun. (b) Total spectral energy density in the magnetic field fluctuations. (c) Angle between the minimum variance direction in b and the background magnetic field B_0. (d)–(i) Fraction of spectral energy density in each of the modes indicated.

each f_{SC} and t is defined by the low pass filtering the field vectors at $f_{SC}/10$. From these field-aligned data, m is determined via the manner described above and the vector quantities subsequently rotated into the corresponding coordinate system. These data are assembled to provide S and the normalized spectral composition in each mode ($\overline{g_i}^2$) is then derived via Equations (3) and (4). As shown in Figure 2(c) the analysis finds rapids variations in θ_m as functions of both f_{SC} and t, yet this rapid variation is not reflected in comparable changes in the composition results shown in the subsequent panels. This invariance demonstrates the insensitivity of the decomposition technique to the specific value of θ_k as discussed above.

When describing the decomposition results shown in Figure 2 our discussion primarily concerns wave observations inside and outside regions of reversed (outward) radial magnetic field without addressing the nature of the generally impulsive field rotations that lead to this topology. While the decomposition identifies them as primarily Alfvénic the 3D nature of these features is not consistent with the plane–wave description implicit in the decomposition technique. With this distinction made, in Figures 2(d)–(i), we find that both inside and outside the reversed radial field regions, the composition is dominated by a broad spectrum of the backward propagating
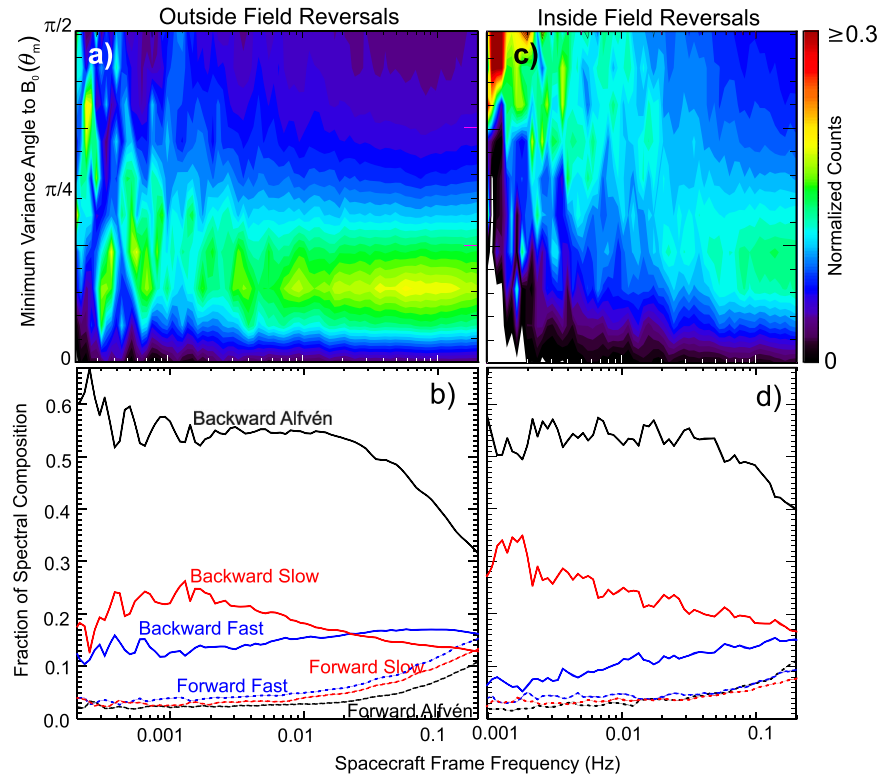
Figure 3. Statistical results compiled over *PSP*s first Perihelion. Panels (a) and (b) show results recorded outside regions of magnetic field reversal while panels (c) and (d) show results recorded within field reversals. Panels (a) and (c) show histograms for the distribution of the minimum variance angle (θ_m) relative to $\boldsymbol{B}_0$ as a function of spacecraft frame frequency. Panels (b) and (d) show the average fractional composition in each of the six MHD modes at each spacecraft frame frequency. Solid lines are backward propagating relative to $\boldsymbol{B}_0$, while dashed lines are forward propagating.

shear Alfvén waves (Figure 2(c)). These backward waves propagate antiparallel to $\boldsymbol{B}_0$, and for positive $\boldsymbol{B}_0$ in spacecraft coordinates, propagate outward. Significantly, the dominate mode remains the backward propagating shear Alfvén wave irrespective of the orientation of $\boldsymbol{B}_0$. For the radial reversals in $\boldsymbol{B}_0$ identified in Figure 2(a) this result indicates that during these intervals the Alfvén wave propagates inward in the plasma frame. This morphology is suggestive of outward propagation from a lower altitude source along corrugated or kinked magnetic field lines. The backward propagating slow mode (Figure 2(i)) provides the bulk of the remaining spectral energy density. At the lowest frequencies surveyed its contribution is anticorrelated and is sometimes comparable to that in the backward Alfvén mode. The spectral contribution from the slow mode is typically enhanced inside and around intervals of reversed radial field where it can make significant contributions over the full frequency range considered. In contrast, enhancements in the fast mode (Figures 2(f) and (g)) are mostly restricted to $f_{SC} \gtrsim 0.01$ Hz and are largest outside those regions of reversed radial field. Intervals containing a large contribution in the fast mode are sometimes observed in regions with high plasma β. The contribution from the forward propagating modes is, in general, much less than that found in the backward propagating waves. Instances of large contributions from the forward modes are occasionally observed, albeit not over the interval shown in Figure 2. The contribution from forward propagation, in general, increases in magnitude with f_{SC}. This dependency becomes more readily apparent in the statistics compiled over the full perihelion pass, as we now consider.

Figure 3 presents the statistical variation in θ_m and the spectral composition over *PSP*'s first perihelion as a function of f_{SC} outside ((a) and (b)) and inside ((c) and (d)) regions of the reversed radial magnetic field. In compiling this figure (and the remaining figures of this work) only those spectral estimates corresponding to wave periods that fit within the boundaries defined by pairs of field reversals enclosing intervals of outward and inward directed radial field are included. As an illustrative example, the enhanced backward slow mode indicated in Figure 2(i) between 03:00 and 03:30 UT at ~3 mHz is not included in the spectral statistics because the corresponding temporal scale exceeds the time between the field reversals shown in Figure 2(a) with which it coincides. The length of intervals between reversals is highly variable (Dudok de Witt et al. 2020) with the range of f_{SC} inside regions of the reversed radial field reduced relative to that outside due to the more limited width of the reversed field regions. The limited statistics at the lowest frequencies in both distributions is likely responsible for the fine structure in Figures 3(a) and (c) rather than representative of features of the true distributions. However, our focus here is on the broader trends, so with these qualifications noted, the 2D histograms in Figures 3(a) and (c) show that θ_m, while broadly distributed from 0 to $\pi/2$, transitions from largely oblique angles at the lowest frequencies surveyed toward a broad peak at $\theta_m \sim \pi/8$ for $f_{SC} \gtrsim 0.01$ Hz. It is also generally the case that θ_m is larger in regions of radial field reversals at the same f_{SC}. The difference in flow speeds inside and outside field reversal regions is insufficient to attribute this difference to the enhanced Doppler shift of the same distribution of $\theta_m(k)$ in each region.
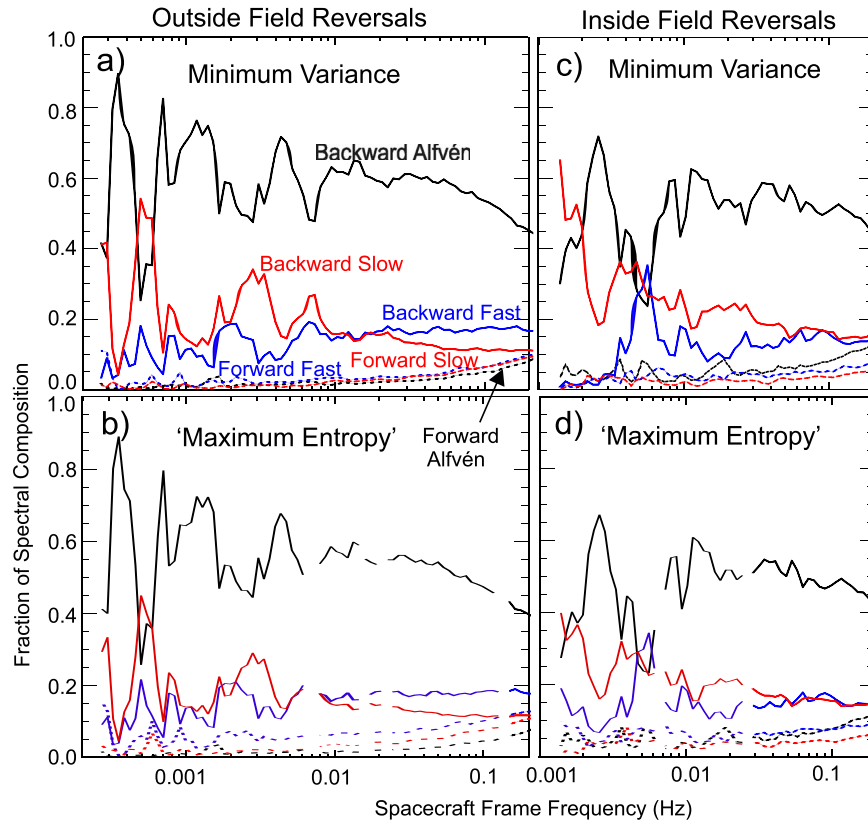
Figure 4. Comparison of averaged composition results from 2018-11-07/00-04 UT derived via the minimum variance ((a) and (c)) and "maximum entropy" approaches ((b) and (d)) outside ((a) and (b)) and inside ((c) and (d)) field reversal regions respectively.

The corresponding statistical averages for spectral composition shown in Figures 3(b) and (d) generally follow the trends exposed by the case study example. The backward propagating Alfvén mode comprises 50%–60% of the observed spectral energy density with a modest enhancement in the field reversal regions. This fraction however progressively drops with f_{SC} for $f_{SC} \gtrsim 0.01$ Hz due to the increasing contribution from the forward propagating modes. The contribution from the backward propagating slow mode is enhanced inside regions of radial field reversal, providing up to 30% of the composition at the lowest frequencies. The fast mode generally constitutes less than 20% of the spectral composition in both the forward and backward propagating modes combined. This mode is most strongly represented outside field reversal regions and at higher frequencies where, for $f_{SC} \gtrsim 0.1$ Hz, both forward and backward propagating modes each provide ~10% of the spectral energy density. In general, the forward propagating modes each contribute $\leqslant$5% over the range of $0.0002 \leqslant f_{SC} \lesssim 0.01$; this is a small but statistically significant value. We will return to consider the origin of these forward propagating modes in the Section 4.

To explore the robustness of these results we have performed an analysis on a small sample of intervals that evaluates $g_i^2(f_{sc}, t; \theta_k)$ and uses the maximum of this distribution for each mode to estimate the most probable contribution to spectral energy density at each f_{sc} and t. This process is a reduced form of the "maximum entropy" technique described by Oscarsson (1994) to estimate the most probable form of the wave distribution function using single point measurements for a specified plasma wave model—in our case single fluid MHD. Figure 4 shows the fractional composition averaged over the

interval shown in Figure 2 using the minimum variance estimate (as implemented above) and the "maximum entropy" result both outside (Figures 4(a) and (b)) and inside (Figures 4(c) and (d)) the field reversal regions. Gaps in the curves shown in Figures 4(b) and (d) are due to failure to locate a clear maximum in $g_i^2(f_{sc}, t; \theta_k)$ in one, or more, of the modes at some time over the averaging interval. Comparing Figure 4(a)–(b) and Figure 4(c)–(d) one finds that with the exception of a small increase in the forward propagating magnetosonic modes in the "maximum entropy" decomposition, the results retuned from both approaches within the degree of estimated uncertainty described earlier are the same. We reserve more extensive implementation of the "maximum entropy" approach for future efforts using a fluid-kinetic model. However, within the single fluid MHD model the near invariance of the spectral estimates returned from both approaches supports the veracity of the composition represented in Figures 2 and 3.

4. Discussion and Conclusion

Figure 5 provides a schematic representation of the field topology and mode composition observed during the first perihelion pass as inferred from the MHD model. The solid black corrugated, or kinked, curve represents the magnetic field, $\boldsymbol{B}_O$, that gives rise to the reversals in radial magnetic field along the trajectory of *PSP* and along which the forward and backward traveling MHD modes identified via the decomposition travel. While these features are largely Alfvénic (Bale et al. 2019; Kasper et al. 2019; Horbury et al. 2020), in our analyses, they contribute to the background in which the modes we identify propagate. The majority of spectral energy density is
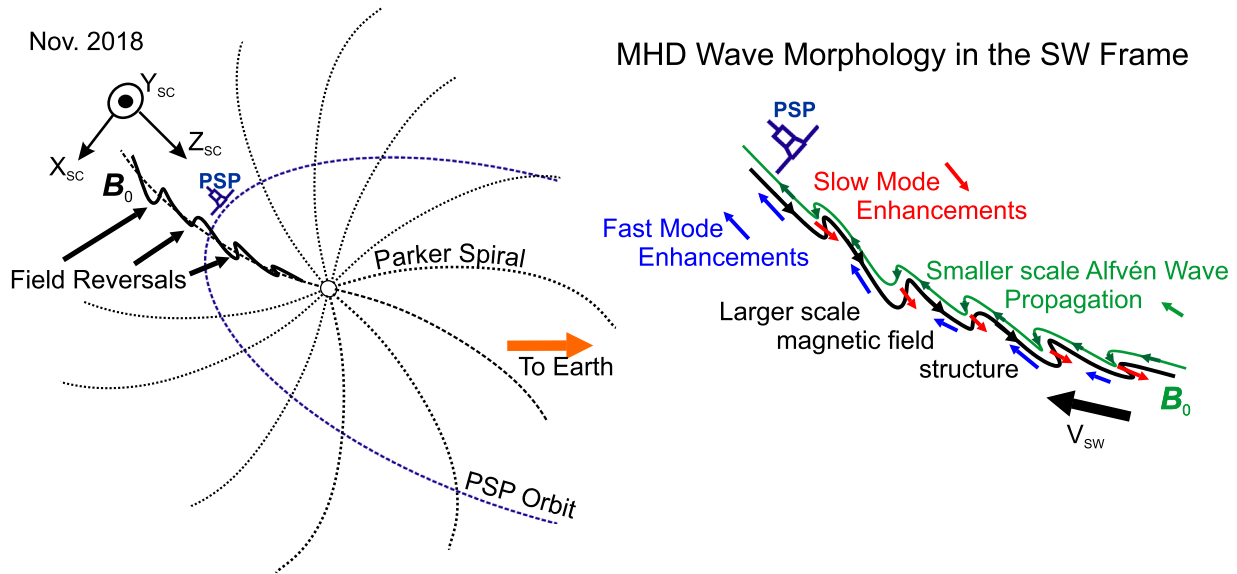
Figure 5. Schematic of MHD wave observations and inferred field geometry over *PSP*s first perihelion in the presence of field reversals (or "switchbacks") represented as kinked magnetic fields. Shear Alfvén waves (green) on scales smaller that the reversals "snake" outward along kinked magnetic field lines (black) and slow mode waves (red) are enhanced inside field reversals, while fast mode waves (blue) occur in regions between field reversals. All waves shown are backward propagating with respect to $\boldsymbol{B}_0$ and are radially outward or inward propagating in the solar wind frame when outside or inside field reversals, respectively.

contained in modes whose wavevector has a component directed opposite (backward) to $\boldsymbol{B}_0$. This is true irrespective of the orientation of $\boldsymbol{B}_0$. For the location of the spacecraft relative to the heliospheric current sheet over the interval considered (Bale et al. 2019) this observation is indicative of a source closer to the Sun radiating wave energy outward. A similar morphology can be derived by assuming a high degree of Alfvénicity and by examining the Elsässer variables (McManus et al. 2020). These backward propagating modes are, in general, dominated by shear Alfvén waves but over short intervals and generally limited ranges in f_{SC}, the contribution from magnetosonic modes can be comparable—this is especially apparent within those intervals where radial B_O reverses and the slow mode is enhanced. These features may be in the form of pressure balance structures (Verscharen et al. 2017). On the other hand, enhancements in fast mode waves occur largely outside those regions of field reversal where they propagate mostly outward, albeit with a comparatively larger inward (forward) component than that the found in the other modes. Over the interval considered there are, however, exceptions to these general trends. This especially concerns the contribution of the fast mode that is sporadically enhanced in both backward and forward propagating sense during intervals of large plasma β.

The statistics represented in Figure 3 indicate a background level in the forward modes of between 3% and 5% over the range of $f_{SC} \lesssim 0.01$ Hz. This fraction increases with f_{SC} at higher frequencies to values of the order of 10% at 0.2 Hz (the highest frequency surveyed). The systematic presence of inward propagation reported in shear Alfvén waves at larger radial distances (e.g., Marsch & Tu 1990) has been attributed to parametric decay and other local instabilities (Primavera et al. 2003; Matthaeus et al. 2004; Bowen et al. 2018) as well as back scatter from inhomogeneities (Velli et al. 1990). While the parametric decay of the backward shear Alfvén mode may account for the occurrence of its forward propagating counterpart at *PSP* it does not account for the same observations in the fast and slow modes. In fact the similarity in the frequency
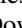
range over which the forward propagation becomes significantly enhanced in all three modes seems more consistent with scattering of the dominant backward modes off the evolving large-scale radial field reversal structures ubiquitous through the interval studied. The increases in forward mode spectral energy densities for $f_{SC} \gtrsim 0.01$ suggest a maximum inhomogeneity scale size for scattering of the order of ∼40,000 km for the observed solar wind speed shown in Figure 1. In this interpretation this size represents an upper limit on the distance along the solar wind direction over which a field reversal from radially inward to outward pointing (or vice versa) occurs. This estimate is qualitatively consistent with the field reversal observations shown in Figures 1 and 2(a) when interpreted as a radial structure advected outward with the solar wind in the manner illustrated in Figure 5.

In summary the results presented in this work characterize the linear mode MHD spectral composition of low-frequency field and plasma variations over *PSP*'s first perihelion pass from 53 to 35 solar radii from the Sun and while on field lines connected to a coronal hole. The analysis decomposes the field and plasma variations both in frequency space (or scale) and MHD mode such that nonlinearities are represented as a superposition of linear modes; however, estimates where $|\boldsymbol{b}|/|\boldsymbol{B}_0|$ is of the order of 1 at a given time and scale are largely eliminated from the statistics. The decomposition approach yields similar results for Alfvénic field variations observed at larger heliospheric distances while simultaneously returning the magnetosonic mode composition from the full set of MHD wave variables. This reveals outward propagating magnetosonic waves primarily composed of the slow mode with spectral energy densities comprising up to 30% of the total wave spectral energy or at most $1/2$ the outward propagating Alfvén wave energy density. It should be noted that these estimates include the contribution to wave energy density from plasma compression, flow, and the magnetic field and are consequently expected to be larger than those returned when the energy density in the magnetic field or flow are alone considered. The invariant dominance of backward mode wave

energy, for the location of the spacecraft over the interval studied, is indicative of outward propagation from a near Sun source along kinked magnetic field lines advected with the solar wind that provide the impulsive radial field reversals characteristic of the environment surveyed by *PSP* over its first perihelion.

ORCID iDs

S. D. Bale ● https://orcid.org/0000-0002-1989-3596
J. C. Kasper ● https://orcid.org/0000-0002-7077-930X
M. Pulupa ● https://orcid.org/0000-0002-1573-7457
T. Dudok de Wit ● https://orcid.org/0000-0002-4401-0943
T. A. Bowen ● https://orcid.org/0000-0002-4625-3332
P. L. Whittlesey ● https://orcid.org/0000-0002-7287-5098
R. J. MacDowall ● https://orcid.org/0000-0003-3112-4201
D. Vech ● https://orcid.org/0000-0003-1542-1302
A. W. Case ● https://orcid.org/0000-0002-3520-4041
M. L. Stevens ● https://orcid.org/0000-0002-7728-0085
K. E. Korreck ● https://orcid.org/0000-0001-6095-2490
D. M. Malaspina ● https://orcid.org/0000-0003-1191-1558

References

Badman, Bale, S. D., Martínez Oliveros, J. C., et al. 2020, ApJS, doi:10.3847/1538-4365/ab4da7
Bale, S. D., Badman, S. T., Bonnell, J. W., et al. 2019, Natur, 576, 237
Bale, S. D., Goetz, K., Harvey, P. R., et al. 2016, SSRv, 204, 49
Balogh, A., Beek, T. J., Forsyth, J. R., et al. 1992, A&AS, 92, 271
Bavassano, B., Pietropaolo, E., & Bruno, R. 2004, AnGeo, 22, 689
Belcher, J. W., & Davis, L., Jr 1971, JGR, 76, 3534
Bowen, T. A., Badman, S., Hellinger, P., & Bale, S. D. 2018, ApJL, 854, L33
Bruno, R., & Bavassano, B. 1991, JGR, 96, 7841
Bruno, R., & Bavassano, B. 1993, P&SS, 41, 677
Bruno, R., & Carbone, V. 2005, LRSP, 2, 4
Bruno, R., & Carbone, V. 2016, LNP, 928
Bruno, R., Bavassano, B., D'Amicis, R., et al. 2006, SSRv, 122, 321
Case, A. W., Kasper, J. C., Stevens, M. L., et al. 2020, ApJS, doi:10.3847/1538-4365/ab5a7b
Chandran, B., Li, B., Rogers, B. N., Quataert, E., & Germaschewski, K. 2010, ApJ, 720, 503
Chen, C. H. K., Klein, K. G., & Howes, G. G. 2019, NatCo, 10, 740
Dudok de Wit, Krasnoselskikh, V. V., Bale, S. D., et al. 2020, ApJS, doi:10.3847/1538-4365/ab5853
Gerschmann, Zurbuchen, T. H., Fisk, L. A., et al. 2012, JGRA, 117, A00M02
Glassmeier, K. H., Motschmann, U., & von Stein, R. 1995, AnGeo, 13, 76
Horbury, T., Woolley, T., Laker, R., et al. 2020, ApJS, doi:10.3847/1538-4365/ab5b15
Howes, G. G., Bale, S. D., Klein, K. G., et al. 2012, ApJL, 753, L19
Huang, J., Kasper, J. C., Vech, D., et al. 2020, ApJS, doi:10.3847/1538-4365/ab74e0
Kasper, J. C., Abiad, R., Austin, G., et al. 2016, SSRv, 204, 131
Kasper, J. C., Bale, S. D., Belcher, J. W., et al. 2019, Natur, 576, 228
Leamon, R. J., Smith, C. W., Ness, N. F., & Wong, H. K. 1999, JGR, 104, 22331
Liu, S., Petrosian, V., & Mason, G. M. 2004, ApJL, 613, L81
Marsch, E., & Tu, C.-Y. 1990, JGR, 95, 8211
Matthaeus, W. H., Minnie, J., Breech, B., et al. 2004, GeoRL, 31, 12803
McManus, M. D., Bowen, T. A., Mallet, A., et al. 2020, ApJS, doi:10.3847/1538-4365/ab6dce
Motschmann, U., Glassmeier, K. H., & Pincon, J. L. 1998, ISSIR, 1, 79
Mozer, F. S., Agapitov, O. V., Bale, S. D., et al. 2020, ApJS, doi:10.3847/1538-4365/ab5e4b
Ofman, L. 2016, in Low-frequency Waves in Space Plasmas, ed. A. Keiling, D.-H. Lee, & V. Nakariakov (Washington, DC: American Geophysical Union), 243
Oscarsson, T. 1994, JCoPh, 110, 221
Primavera, L., Malara, F., & Veltri, P. 2003, in AIP Conf. Proc. 679, SOLAR WIND TEN, ed. M. Velli et al. (Melville, NY: AIP), 505
Richter, A. K., & Marsch, E. 1988, AnGeo, 6, 319
Roberts, D. A. 2010, ApJ, 711, 1044
Samson, J. C., & Olson, J. V. 1980, GeoJ, 61, 115
Shi, M. J., Xiao, C. J., Li, Q. S., et al. 2015, ApJ, 815, 122
Tsurutani, B. T., Lakhina, G. S., Sen, A., et al. 2018, JGRA, 123, 2458
Tu, C.-Y., & Marsch, E. 1994, JGR, 99, 481
Tu, C.-Y., & Marsch, E. 1995, SSRv, 73, 1
Velli, M., Grappin, R., & Mangeney, A. 1990, CoPhC, 59, 153
Verscharen, D., Chen, H. K., & Wicks, R. T. 2017, ApJ, 840, 106
Yao, S., He, J.-S., Marsch, E., et al. 2011, ApJ, 728, 146